catalysts

MDPI

Article

MgCr-LDH Nanoplatelets as Effective Oxidation Catalysts for Visible Light-Triggered Rhodamine B Degradation

Susanginee Nayak * and Kulamani Parida *

Centre for Nano Science and Nano Technology, Institute of Technical Education and Research (ITER), Siksha 'O' Anusandhan Deemed to be University, Bhubaneswar 751030, Odisha, India

* Correspondence: susanginee@gmail.com (S.N.); kulamaniparida@soauniversity.ac.in or paridakulamani@yahoo.com (K.P.); Tel.: +91-674-2351777 (K.P.)

Abstract: In this work, we successfully exfoliated MgCr-(NO_3^-) LDH with large purity by a simple formamide method followed by post-hydrothermal treatment and characterized by different physico-chemical techniques. The UV-DRS study persuades the red-shifted absorption band and suitable band gap of MgCr-(NO_3^-) LDH for optimum light harvestation ability related to the optical properties. Alternatively, the production of elevated photocurrent density of MgCr-(NO_3^-) LDH (3:1, 80 °C) in the anodic direction was verified by the LSV study, which further revealed their effective charge separation efficacy. These MgCr-LDH nanosheets (3:1, 80 °C) displayed the superior Rhodamine B (RhB) degradation efficiency of 95.0% at 0.80 kW/m^2 solar light intensity in 2 h. The tremendous catalytic performances of MgCr-LDH (3:1, 80 °C) were typically linked with the formation of surface-active sites for the charge trapping process due to the presence of uncoordinated metallocenters during the exfoliation process. Furthermore, the maximum amount of the active free atoms at the edges of the hexagonal platelet of MgCr-LDH causes severance of the nanosheets, which generates house of platelets of particle size ~20–50 nm for light harvestation, promoting easy charge separation and catalytic efficiency. In addition, radical quenching tests revealed that h^+ and •OH play as major active species responsible for the RhB degradation.

Keywords: LDH; exfoliation; nanosheets; oxidation; photocatalysts

Citation: Nayak, S.; Parida, K. MgCr-LDH Nanoplatelets as Effective Oxidation Catalysts for Visible Light-Triggered Rhodamine B Degradation. *Catalysts* **2021**, *11*, 1072. https://doi.org/10.3390/catal11091072

Academic Editors: Ioan-Cezar Marcu and Octavian Dumitru Pavel

Received: 12 July 2021
Accepted: 31 August 2021
Published: 3 September 2021

1. Introduction

Layered structure material represents an emerging class of two-dimensional (2D) materials that acquire sheet-like morphology with the thickness of single or few-layered atoms [1–3]. The importance of layered materials is credited due to their rich interlayer chemistry, such as intercalation and ion exchange properties, which modified their electronic and optical properties. There are lot of many-layered solid materials with few-layer, single-layer, or stacked-layered structures that have been identified as such layered double hydroxide (LDH) [3–9], layered metal hydroxides [10], layered graphene oxide [4,9], and layered graphitic carbon nitride (g-C_3N_4) [11–14], in photocatalytic dye degradation and energy conversion reactions. Amongst these, LDHs have been considered as one of the most efficient photocatalysts in producing clean H_2 energy along with environmental abatement following a green technological aspect. Although the direct semiconducting capability of LDH is very much restricted, its lamellar structure smooths the photoinduced electron transfer from bulk to the surface, which is useful in water splitting, and the photo-generated holes are thereof involved in the pollutant degradation [15,16]. Normally, LDHs represents a group of anionic layered materials consisting of positively charged layers with interlayer anions and H_2O molecules for charge recompense, which is widely used as catalysts, catalyst support, ion exchangers, and electrocatalytic and photocatalytic materials [5]. The generic formula of LDHs is $[M(II)_{1-x}M(III)_x(OH)_2]^{x+}[A^{n-}{}_{x/n}\cdot mH_2O]^{x-}$, where M(II) and M(III) specify the metal atoms and A^{n-} represents the anions, n is the charge upon interlayer anion, m is amount of H_2O, and $x = M^{III}/(M^{II} + M^{III})$. The atomic arrangement

of LDHs is correlated to that of brucite-like layers of $Mg(OH)_2$, and the development of excess charge owing to the inclusion of M(III) cations is balanced by the intercalation of A^{n-} together with the presence of H_2O in the interlayer gallery. Stable LDHs requisites M(II)/M(III) ratio among 2:1, 3:1, and 4:1, where x lies in the range of $0.20 < x < 0.33$. However, the bulk LDHs is restricted to certain applications owing to the detachment of the inner portion of the layer host structure. 2D LDH usually crystallizes into small hexagonal platelets or house-of-card morphology owing to their 2D layered structure possessing large surface area and could be simply prepared with NO_3^- anions by co-precipitation method. An intriguing feature of 2D material is their potential to exfoliate/delaminate into resultant uni/multi-lamellar crystallites or nanosheets (NS) having unusual structural aspects, which are of critical 2D anisotropy [17]. According to this reason, LDHs could be exfoliated into single/multiple 2D NS of thickness ~1 nm, and that may be used as building block for various functional nanoheterostructures materials with positively charged NS framework in comparison to positively charged montmorillonite framework [18].

In order to optimize the formamide exfoliation procedure of strongly bound positively charged NS of LDHs, several factors have been verified in the recent days; e.g., chemical nature and composition of the 2D-brucite-like layers [19,20], organic solvents systems (acrylates, butanol, toluene, etc.) [21,22], charge of anions [22], drying procedure [23], water content [24], hydrothermal treatment [25], and morphological variation [20]. A challenge for the thorough investigations is associated with the sufficient control on the interlayer interaction with brucite-like layers, stacking fault, and inclusion of polytype pattern. The substitution of M(II) by M(III) cation in binary LDHs induces excess layer charge and affects the interaction with the polar solvent formamide molecules. For illustration, $Mg_{1-x}Al_x(OH)_2(glycinate)_x.\ mH_2O$, x = 0.25 exfoliates better in formamide [19]. During the exfoliation process, most specifically, the intercalated or surface bound solvent molecules connected via H-bonding with the interlayer anions and the –OH group of the metal hydroxide layers and electrostatically interacted with the positively charged 2D LDH NS. The interlayer gallery expansion is dependent upon the layer charge density and at low layer charge density; the basal spacing is tightly bound with horizontal orientation of NO_3^- ions. Alternatively, the NO_3^- anions and H_2O molecules are oriented out of the horizontal plane at elevated layer charge density, enhancing gallery height extension. However, exfoliation is triggered by hydration process but much improved by tuning hydrothermal temperature, time, and at fixed compositions, e.g., x = 0.25.

Herein, the present work is related to reference [7], and our aim was to promote the exfoliation of MgCr-LDH (Mg(II): Cr(III) = 2:1, 3:1, and 4:1) using the formamide method followed by post-hydrothermal treatment (70, 80, and 90 °C). By adopting this robot synthetic methodology, the MgCr-(NO_3^-) LDH (3:1, 80 °C) preserved house-of-cards or nano-platelet-like morphology, which clearly disclosed a high degree of exfoliation of the materials. Consequently, MgCr-LDH (3:1, 80 °C) displayed 95.0% RhB degradation in 2 h under visible light exposure.

2. Results and Discussion

2.1. XRD Characterization

PXRD proceeded to recognize the crystal structure, crystallinity, and phase purity of the materials [26]. In the process of hydrolysis of Mg/Cr nitrate solution by aqueous NaOH solution and formamide, the crystal clear MgCr-LDH dispersion displayed the occurrence of colloidal MgCr-LDH. Then, centrifuging the colloidal MgCr-LDH dispersion yielded an MgCr-LDH gel containing freely and arbitrarily stacked LDH NS. Later, post-hydrothermal treatment of these MgCr-LDH gels produced uni/multilayer NS. Figure 1a (i–iii), displays the variation of characteristic diffraction peaks of MgCr-LDH (2:1), MgCr-LDH (3:1), and MgCr-LDH (4:1) without hydrothermal treatment along with hydrothermal-treated samples at different temperatures (70, 80, and 90 °C), which clearly resembled exfoliated LDH NS with a small enough crystalline nature (Figure 1a (iv–vi)). The XRD patterns of the as-synthesized MgCr-LDH (3:1) samples without hydrothermal treatment exhibit

broadening of peak at 2θ = 30° to 60.4° owing to the presence of formamide and corresponds to the (012) and (110) planes, respectively (Figure 1a (ii)). The absence of (003) and (006) characteristic planes in MgCr (3:1) material reveals the exfoliation of bulk MgCr-LDH. Similarly, MgCr-LDH (2:1) and MgCr-LDH (4:1) follow the similar XRD pattern as that of MgCr-LDH (3:1) with a slight appearance of the (006) plane in MgCr-LDH (4:1). The (006) planes in the PXRD pattern of MgCr-LDH (3:1, 80 °C) at lower 2θ~11–23° revealed broad and symmetrical basal reflections, while the spiky and asymmetrical reflections of (012) and (110) were expressed at higher 2θ~34–66°, respectively. The broad (006) and spike (110) planes of MgCr-LDH (3:1, 80 °C) could be correlated with the interlayer height differences and stacking disorder of distinct NS in materials [27,28], whereas the rest of crystalline plane was absence in the PXRD pattern of hydrothermally-treated MgCr-LDH (Figure 1b (v)). The interlayer spacings (d) were deliberate via Braggs law, nλ = 2d sin (θ), in which n = 1, λ is the wavelength of the target and θ is the angle of incidence. The d value of MgCr-LDH (3:1, 80 °C) was found to be 0.46 nm corresponding to d (006) plane and NO_3^- as interlayer anion. Alternatively, the d value of MgCr-LDH (3:1) without hydrothermal was found to be 0.16 nm corresponding to d (110) plane as there were absence of (003) and (006) plane in the PXRD pattern of the material. Hence, hydrothermal temperature played a major role and dramatically altered the crystal growth of the exfoliated MgCr-LDH NS, and the utmost crystallinity was noted at 80 °C for MgCr-LDH (3:1) [29].

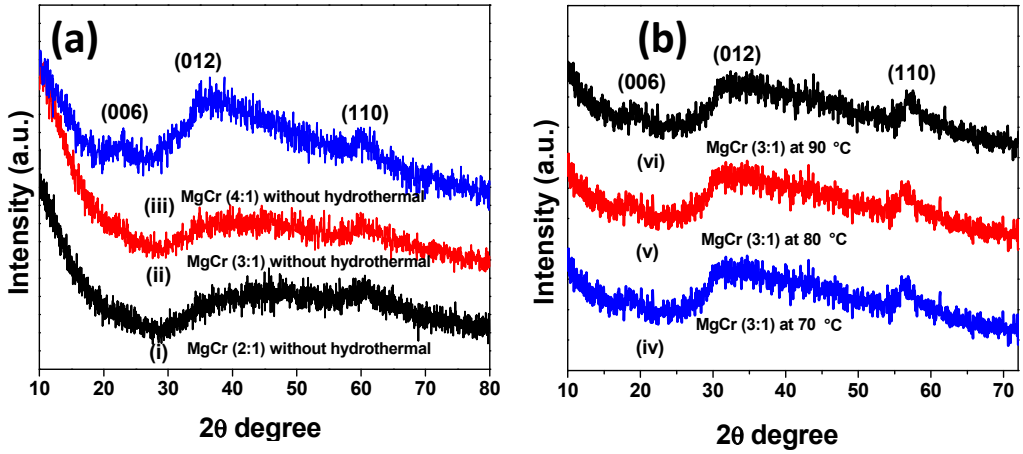

Figure 1. XRD spectra of exfoliated MgCr-LDH (2:1), MgCr-LDH (3:1), and MgCr-LDH (4:1) without hydrothermal ((**a**) (i–iii)); exfoliated MgCr-LDH (3:1) at different hydrothermal temperature of 70, 80, and 90 °C ((**b**) (iv–vi)).

2.2. Morphological Analysis

TEM images were acquired to trace out the arrangement of the LDH uni/multi-lamellar NS (Figure 2) [30]. In the moderately dissipate area, the MgCr-LDH lamellae (3:1, 80 °C), possess platelet like shape oriented at random with house-of-card morphology (Figure 2a,b). Contrary to the typical hexagon, at mild hydrothermal temperature of 80 °C, the elevated amount of dynamic in free atoms at the edges of the hexagonal platelet causes intersection of the NS, which generates house of platelets type morphology of MgCr-LDH as shown in Figure 2b. Figure 2c reveals distinct lattice distance ~0.38 nm in MgCr-LDH (3:1, 80 °C), which is approximately related to the (006) plane of the 2D MgCr-LDH nanocrystals. The particle diameter of MgCr-LDH (3:1, 80 °C) NS is expected to be average size of 20–50 nm. Furthermore, the morphology of MgCr-LDH (3:1, 80 °C) NS was verified with FESEM analysis. In Figure 2c,d, the morphology of MgCr-LDH (3:1, 80 °C) was composed of irregular matrix and aggregated into larger nanoparticles with rough and porous surface during mild hydrothermal treatment at 80 °C. This might be due to the hydrothermal treatment effect on MgCr-LDH (3:1) materials. Nevertheless, the TEM image of MgCr-LDH (3:1, 80 °C) easily revealed their exact sheet-like morphology

of hexagonal nanoplatelets, which are of distinctive features of exfoliated LDH material, and approximately matching with the XRD outcome. Additionally, the EDX analysis of MgCr-LDH (3:1, 80 °C) as shown in Figure 2c confirms that the system contains all the elements like Mg, Cr, and O without any impurity, which proves its compositional purity.

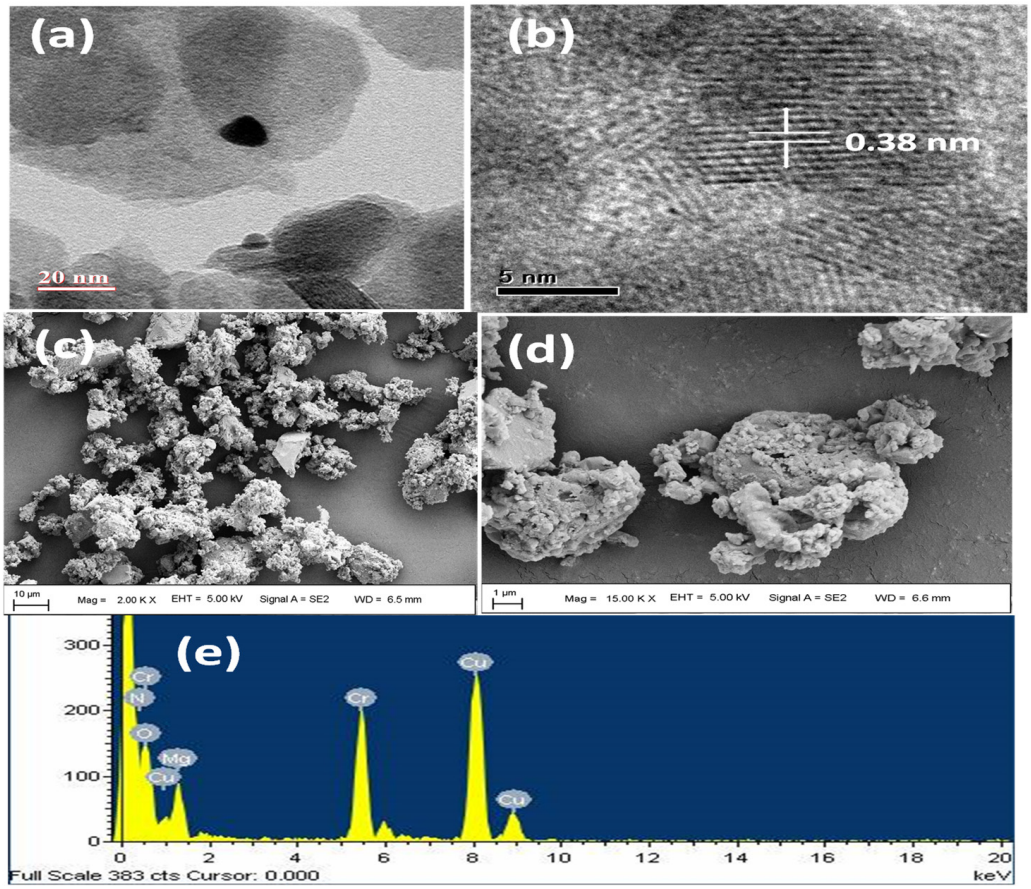

Figure 2. (**a**) TEM morphology of exfoliated MgCr-LDH (3:1, 80 °C), (**b**) lattice fringe of MgCr-LDH (3:1, 80 °C) as detected from HR-TEM image analysis, (**c**,**d**) FESEM morphology of MgCr-LDH (3:1, 80 °C), and (**e**) EDX spectrum of MgCr-LDH (3:1, 80 °C).

2.3. Optical Study

The electronic and optical characteristic properties of the exfoliated MgCr-LDH (2:1, 3:1, 4:1) NS without hydrothermal treatment and MgCr-LDH (3:1) NS with hydrothermal treatment (70, 80, and 90 °C) were determined by UV-Vis DRS spectroscopy technique (Figure 3a). The Figure 3a clearly reveals that each MgCr-LDH photocatalyst possess sufficient potential to absorb visible light and displayed remarkable increase in the absorption intensity, which indicated the enhanced excitonic charge pairs partition efficiency of the resultant materials. In concise, MgCr-LDH (3:1) without hydrothermal displayed broad absorption band within 300–500 nm owing to the ligand to metal charge transfer (LMCT) as O2p → Cr-3d-t_{2g} and absorption band at 500–700 nm is assigned to the 2Eg (D) → $2T_{2g}$ spin allowed transition of Cr^{3+} in the tetrahedral coordination sites [9,26]. Specifically, the gradual increases in the red shift of the absorption band in MgCr-LDH (3:1) are owing to the increase in Cr^{3+} content in the brucite-like host layers. The exfoliation of MgCr-LDH during mild hydrothermal treatment causes severance and folding of NS with formation of tunnels of hexagonal plates, which acts as light harvestation antenna and triggers electronic transition in the respective orbital of the metallocenters in the catalysts. Importantly, the absorption edge of MgCr-LDH (3:1, 80 °C) moved towards a longer wavelength with broad and intense absorption from 400 to 800 nm, which is due to the reduced thickness

of the exposed atomic sites of the nanolayers that minimized the charge transfer distance and endorsed for effective compilation of charge concentrated over the conductive NS. Furthermore, the inimitable structure in MgCr-LDH (3:1, 80 °C) endorsed light to scatter frequently inside the structure to increase the optical distance and enhance light absorption capacity. In addition, the atomically reduced thickness of the exposed atomic sites of the uni/multi-nanolayers of MgCr-LDH (3:1, 80 °C) NS is another factor responsible for the broad and intense visible light absorption capability within 400–800 nm.

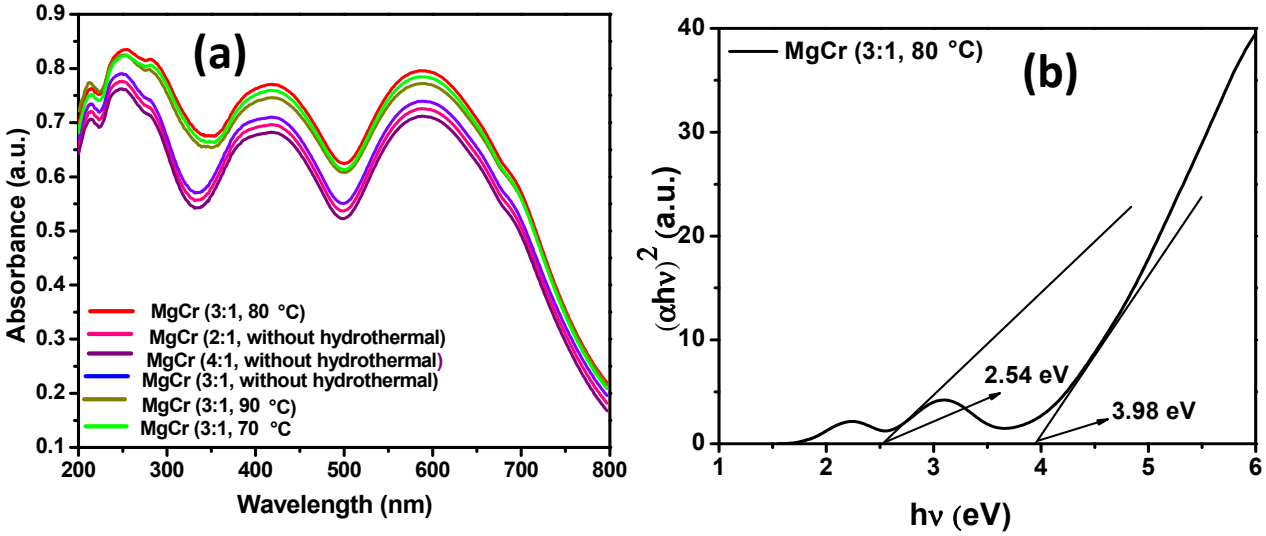

Figure 3. (**a**) UV-Vis DRS spectra of the series of exfoliated MgCr-LDH (2:1, 3:1, 4:1) without hydrothermal and MgCr-LDH (3:1) with hydrothermal treatment of 70, 80, and 90 °C. (**b**) Band gap energy of MgCr-LDH (3:1, 80 °C) as derived from Kubelka–Munk equation through Tauc plot.

The band-gap energy of MgCr-LDH (3:1, 80 °C) can be deliberate by Tauc plot as reported earlier following the Kubelka–Munk Equation (1) [5–13].

$$(\alpha h\nu)^{1/n} = A(h\nu - E_g) \quad (1)$$

where ν and α are the light frequency and adsorption coefficient, respectively

Figure 3b shows two types of band-gap energy resides in MgCr-LDH (3:1, 80 °C), which is of 2.54 (E_g1) and 3.98 eV (E_g2) due to the presence of LDH phase, and falls under directly allowed transition. In addition, the E_g1 can also be assigned to the direct electronic transition from O2*p* to Cr*nd* levels of MgCr-LDH [12]. Furthermore, the E_g2 of MgCr-LDH samples can be assigned to the existence of electronic transition from O2*p* to Mg*ns*/*np* [12].

2.4. FTIR Study

FTIR plot of MgCr-LDH (3:1, 80 °C) is represented in Figure 4 [31]. The sample displayed a broad absorption band at around 3374 cm^{-1}, which signifies the occurrence of -OH group of H_2O molecules [32]. Similarly, the two distinct bands at 1639 and 1440 cm^{-1}, corresponded to the stretching mode of vibration in Mg-O and bending mode of vibration in adsorbed H_2O over MgCr-LDH surface [32]. The absorption band at lower frequency level of 1000 cm^{-1} corresponds to M–O (Mg–O, Cr–O) and M–O–M (Mg–O–Cr) vibrations, respectively [33]. This functional band gives strong evidence of the formation of MgCr-LDH samples.

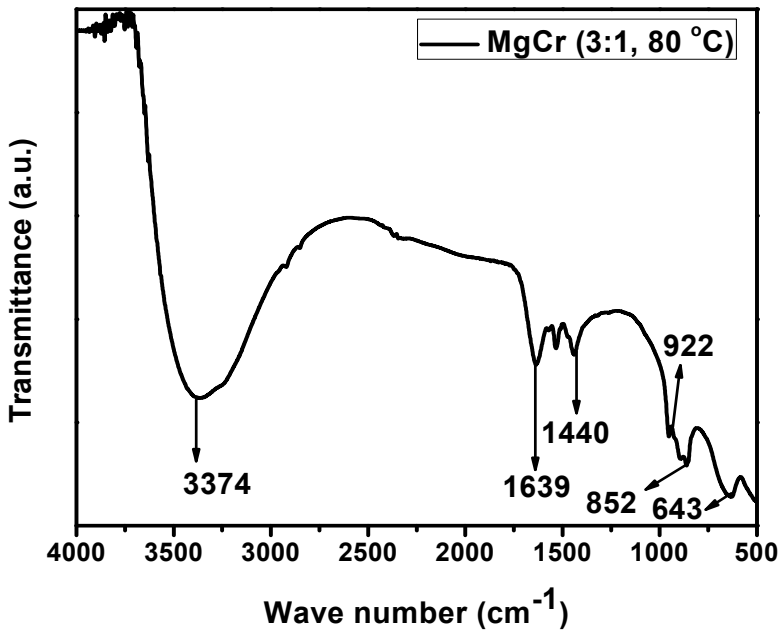

Figure 4. FTIR spectrum of exfoliated MgCr−LDH (3:1, 80 °C).

2.5. Electrochemical Study

LSV study of MgCr-LDH (3:1, 80 °C) samples was conducted in a potential panel of −1.0 to 1.2 V, using 0.1 M Na_2SO_4, and scan rate of 10 $mV \cdot s^{-1}$ to reveal the photocurrent retaliation of the as-synthesized catalysts. Figure 5 exposes the photocurrent capacity measures under dark and light environments. As shown in Figure 5, MgCr-LDH (3:1, 80 °C) could be able to produce current density of 1.20 $\mu A/cm^{-2}$ under light exposure. The progress of the photocurrent in the anodic direction shows that all the MgCr-LDH samples filling the properties of n-type semiconductor [11]. The oxidation peak intensity decreases gradually at optimal loading density of Cr^{3+} in MgCr-LDH (3:1) and further mild hydrothermal treatment at 80 °C provides compact NS structure of MgCr-LDH, where the oxidation peak of $Cr \rightarrow Cr^{3+}$ decreases gradually and disappear, suggesting the enhance stability of MgCr-LDH (3:1, 80 °C) in the nanostructure. The enhanced stability of MgCr-LDH (3:1, 80 °C) causes superior visible light driven photocatalytic activity. The flat band potential of the entire MgCr-LDH sample was detected at −0.60 V vs. Ag/AgCl, pH = 6.5. The flat band potential is directly correlated to baseline of the conduction band (CB) of an n-type semiconductor [11]. As 2.54 eV is the primary E_g of MgCr-LDH, the corresponding valence band maximum (VB) was +1.94 V. Particularly, electrode potential was transformed to NHE by the subsequent Equation (2) [34]:

$$E(\text{NHE}) = E(\text{Ag/AgCl}) + E^0(\text{Ag/AgCl}) + 0.059\text{pH} \quad (2)$$

Hence, CB and VB of MgCr-LDH in NHE scale were determined to be −0.01 and +2.53 V. Similarly, the dark current measurement of MgCr-LDH (3:1, 80 °C) showed a slight incremental current density as compared to light current density.

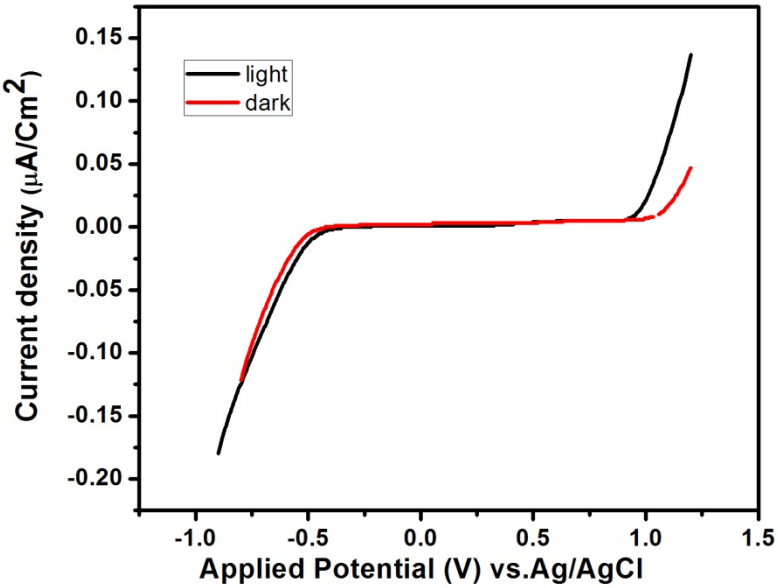

Figure 5. Light and dark current density of MgCr−LDH (3:1, 80 °C).

2.6. Photocatalytic RhB Degradation Activity

The RhB degradation activity of MgCr-LDH samples was studied under solar light exposure. Self-degradation study of RhB was performed by exposing under the solar energy for 30 min, and the results showed that the RhB self-degradation was roughly insignificant. Furthermore, the adsorption study of the catalyst was performed under dark condition for 30 min. The RhB degradation study was activated by dispersion of 0.03 g of the catalyst in 20 ppm of RhB (20 mL) under solar energy for 120 min. The exfoliation of MgCr-LDH under mild hydrothermal condition generates uncoordinated metallocenters and dense amount of free atoms at the edges of hexagonal platelet responsible for oxygen related vacancies and causes intersection of the NS for enhancing light harvestation ability of the materials and corresponding exciton separation efficiency directly or indirectly responsible for the photooxidation of RhB to non-toxic products. The RhB photodegradation activities of all of the as-synthesized MgCr-LDH samples were measured in accordance with the following Equation (3):

$$\text{Photodegradation rate (\%)} = (C_0 - C/C_0) \times 100 \quad (3)$$

The order of intensification of RhB degradation for series of MgCr-LDH was 75% (MgCr 4:1), 85% (MgCr 2:1), 90% (MgCr 3:1), 93% (MgCr 3:1, 70 °C), 95% (MgCr 3:1, 80 °C), and 91% (MgCr 3:1, 90 °C), respectively (Figure 6a). These outcomes evidently show that (MgCr 3:1, 80 °C) exhibits enhanced RhB degradation. In addition, an excess substitution of Cr^{3+} to Mg^{2+} (MgCr 4:1) results decreases in activity because of the blocking of the reactive phases of MgCr-LDH. The rate of RhB degradation and related spectral changes of absorbance are depicted in Figure 6b. MgCr (3:1, 80 °C) shows excessive potential for maintaining higher stability approximately to the extent of 3 cycles (Figure 6c) than other as-prepared materials as discussed so far. The degradation activity results are in fine matching with the characterization results.

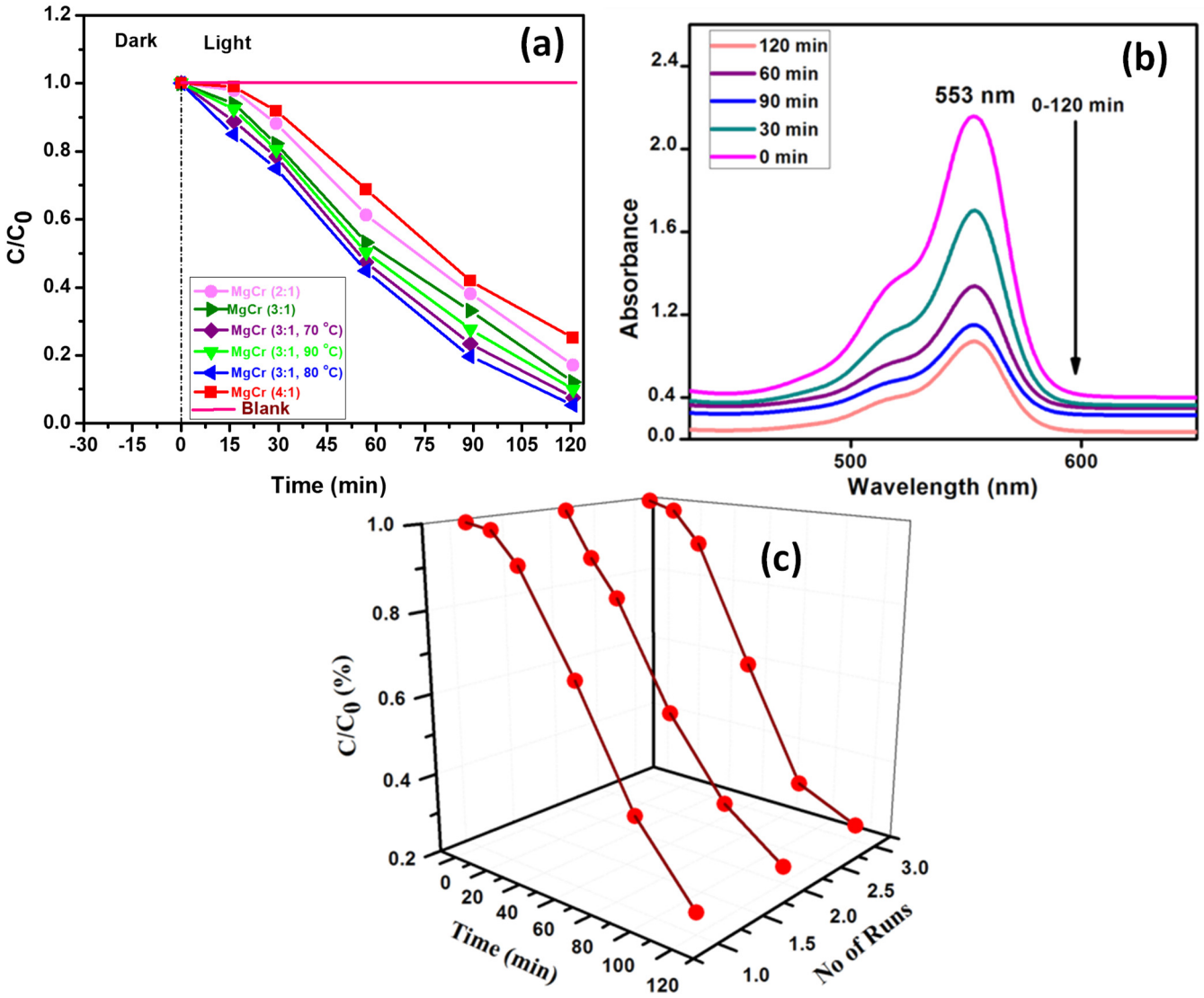

Figure 6. (**a**) Photocatalytic degradation rate of RhB over variant of MgCr−LDH samples. (**b**) Spectral alteration of RhB absorption in different time interval by MgCr 3:1, 80 °C. (**c**) Stability test of MgCr 3:1, 80 °C for three different cycles.

2.7. Kinetics of the RhB Degradation

The kinetics of RhB degradation follows pseudo-first-order and the experimental data were fitted to the Langmuir−Hinshelwood kinetic model using the following Equations (4) and plotted in Figure 7a:

$$\ln C_0/C = kt \quad (4)$$

The *k* denoted as the apparent rate constant. The rate constant (k) of the RhB degradation reaction for different MgCr-LDH samples was calculated by linear fitting of the ln (C_0/C) vs. time plot (Figure 7a) and consequently, the measured slope of ln (C_0/C) vs. time plot provides the value of k. The k value depicted in Table 1 clearly shows that RhB degradation for MgCr-LDH based samples follows pseudo-first order kinetics in Langmuir−Hinshelwood model. The fitted line parameters related to the regression coefficient (R^2) are also given in Table 1.

The superior rate constant value of MgCr 3:1, 80 °C (0.02361 min^{-1}), reveals its great potential as unilamellar NS towards environmental oxidative reactions.

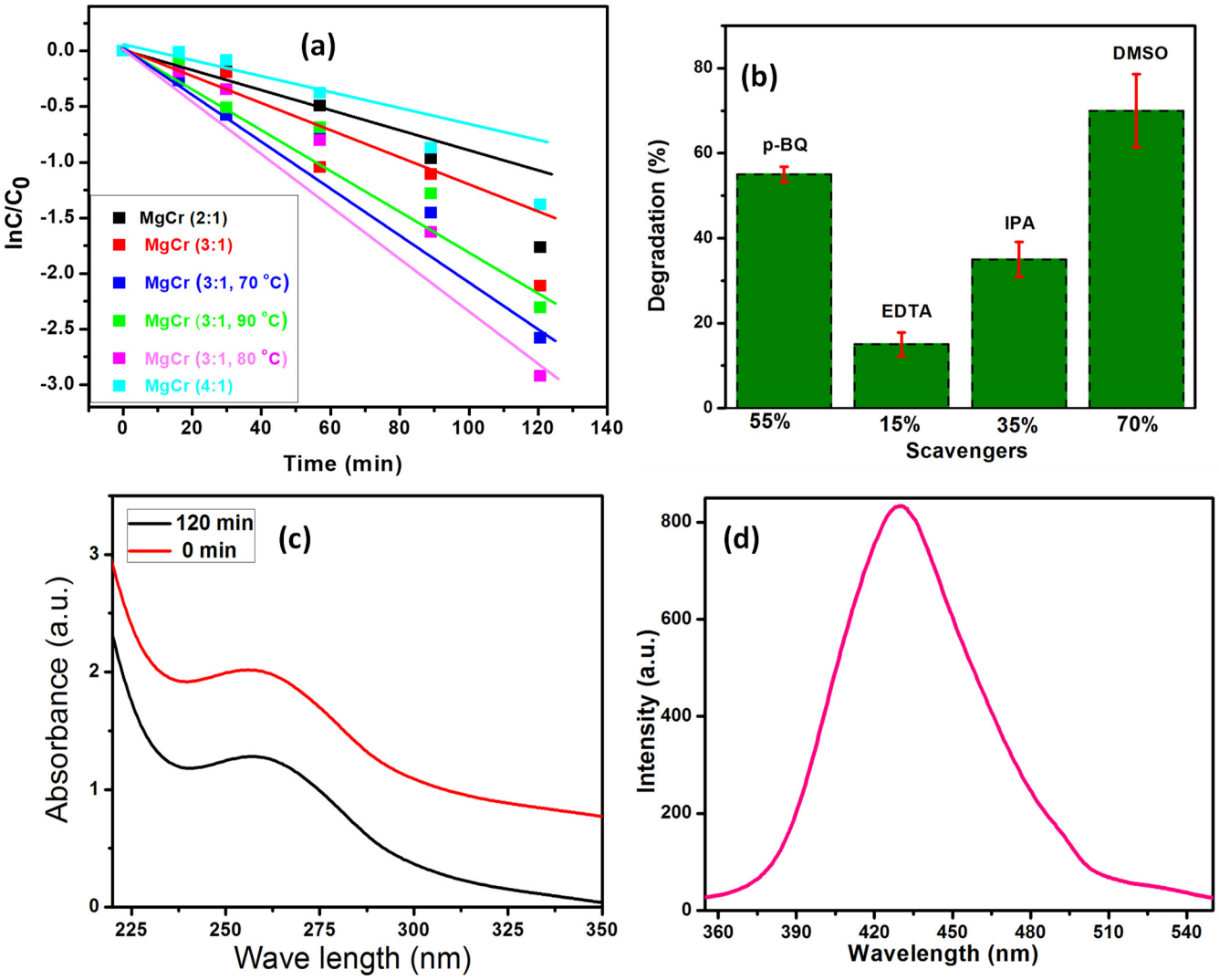

Figure 7. (**a**) Kinetics of RhB degradation by linear fitting of C_0/C vs. time using a series of exfoliated MgCr−LDH samples. (**b**) Histogram showing % of degradation using different scavenging agents. (**c**) Absorbance plot of NBT by MgCr−LDH (3:1, 80 °C). (**d**) PL spectra of MgCr−LDH (3:1, 80 °C) by TA.

Table 1. Rate constant and regression co-efficient value of exfoliated MgCr-LDH NS.

Catalyst	Rate Constant (min^{-1})	R^2
MgCr (2:1)	0.01467	0.93
MgCr (3:1)	0.01739	0.92
MgCr (3:1, 70 °C)	0.01998	0.93
MgCr (3:1, 80 °C)	0.02361	0.93
MgCr (3:1, 90 °C)	0.01836	0.94
MgCr (4:1)	0.01193	0.94

2.8. Scavenger Study for the Radicals

The scavengers taken active part in the RhB degradation study was examined by distinct trapping reagents as para-benzoquinone (p-BQ), dimethyl sulfoxide (DMSO), isopropanol (IPA), and ethylenediaminetetraacetic acid (EDTA) for scavenging superoxide ($\bullet O_2^-$), electron (e^-), hydroxyl ($\bullet$OH), and hole (h^+) radicals, sequentially. In the experiment process, 5 mM of each trapping agent was incorporated to 20 mL of 20 ppm RhB added with 0.03 g of catalyst and set for degradation reactions. The scavenger test results shows an increased rate of RhB degradation (15, 35, 55, 70%) with addition of EDTA, IPA,

p-BQ, and DMSO scavenging reagents, as depicted in Figure 7b. This result shows the participation of hole and hydroxyl radicals as primary and superoxide as secondary active species for RhB degradation process.

2.9. Confirmatory Test for $\bullet O_2^-$ Radicals

The $\bullet O_2^-$ radical was confirmed via a nitroblue tetrazolium (NBT) test [35]. Then, NBT was used to determine dense of $\bullet O_2^-$ and disclose the photodegradation efficiency of MgCr-LDH. Figure 7c shows no such extent of variation in the NBT concentration by MgCr-LDH, before and after the RhB photodegradation reactions, which reveals that CB potential of MgCr-LDH is not sufficient to directly produce $\bullet O_2^-$ radicals.

2.10. Confirmatory Test for •OH Radicals

Terephthalic acid (TA) PL probe was utilized for the detection of •OH radical [36]. TA directly reacts with the •OH radical, producing 2-hydroxyterephthalic acid (TAOH) by emission band at 426 nm for excitation at 315 nm. Then, a ~0.02-g catalyst was supplied to 0.004 M of NaOH solution consisting of 20 mL of TA, and subsequently the suspension was manifest to solar energy for 2 h. Afterward, intense PL peak of TAOH solution quantify the •OH radical formed through photooxidation reactions. The maximum intensity of TAOH peak extends the highest percentage of •OH formation. Figure 7d shows the formation of primary •OH radicals in RhB degradation catalyzed by MgCr-LDH.

2.11. Mechanism of RhB Degradation by MgCr-LDH

The mechanistic path of RhB degradation by using MgCr-LDH catalyst (Figure 8), could be clearly elucidated in terms of structural and morphological features, together with band gap sequence, and active sites, which correlated to the formation of exfoliated NS with photoinduced carrier charge separation for enhanced activity. The apparent enhancement in the photocatalytic RhB degradation over MgCr-LDH is owing to the formation of constant layer charge density, morphological aspects by mild hydrothermal temperature, and surface-active sites during the exfoliation process. Normally, the exfoliation rate decreases at a lower x = 0.2, due to tight interlayer gallery for which the polar interactions towards formamide are reasonable owing to low layer charge density. Though Columbic/electrostatic interactions are considered as an extraneous parameter in LDH containing divalent anion that limits the rate of intercalation, but we noticed the well exfoliation of MgCr-(NO_3^-) LDH at x = 0.3, and provided maximum space for formamide intercalation and consequently increases the basal spacings. It is further noted that high layer charge density could certainly result in strong interaction with formamide, and in this energy balance process, the electrostatic interactions may stabilize the LDH compound. Further MgCr-(NO_3^-) LDH at x = 0.3 provided platelets such as morphology as revealed from TEM image. It is also expected that the degree of exfoliation of $Mg^{II}_{0.9}Cr^{III}_{0.3}$ $(OH)_2(NO_3)_{0.3}$. nH_2O reached to approximately complete exfoliation by post-hydrothermal treatment [13]. Further XRD also revealed a clear node of (006) plane considerably on hydrothermal post-treatment, in context to Cr(III) proportion. This shows a homogeneous allocation of H_2O molecules and out of plane NO_3^- ion orientation and causes interlace crystallites. The LSV analysis also confirmed that MgCr-LDH (3:1, 80 °C) possess an intrinsic n-type characteristic properties of materials. By utilizing the Tauc plot (Figure 3b) derived from the Kubelka–Munk equation and LSV plot (Figure 5), the CB and VB position of MgCr-LDH (3:1, 80 °C) was found to be −0.01 and +2.53 V, corresponding to E_g of 2.54 eV, respectively. Further, MgCr-LDH (3:1, 80 °C)-acquired nano-platelets slanted at random (TEM image) and these morphological features of MgCr-LDH harvests light energy with reflection at the core of tunneling of intersected NS for superior activities. Under visible light exposure, photoexcited charge pairs were generated over the surface of MgCr-LDH. In this way, the migration and separation of photoinduced carriers charge pairs is due to the presence of surface-active sites at nanometric region for electron and hole hopping process. However, the CB position of MgCr-LDH (−0.01 V vs. NHE) is

insufficient for the production of $\bullet O_2^-$ and $\bullet HO_2$ ($E^{\Theta}(O_2/\bullet O_2^-)$ = −0.33 eV vs. NHE) and $E^{\Theta}(O_2/\bullet HO_2$, −0.05 eV vs. NHE) [15,37]. Alternatively, the depth VB position of MgCr-LDH (+2.53 V vs. NHE) was relatively sufficient for the direct oxidation reaction of holes with adsorbed H_2O molecules to form •OH radicals $E^{\Theta}(\bullet OH/OH^-$ = +1.99 eV vs. NHE) [38]. These concepts were verified by the scavenger test, where h^+ were of the primary active-species in MgCr-LDH, which were responsible for the photodegradation of RhB. Consequently, these •OH radicals reacted with RhB over the surface of MgCr-LDH (3:1, 80 °C) to produce non-toxic products.

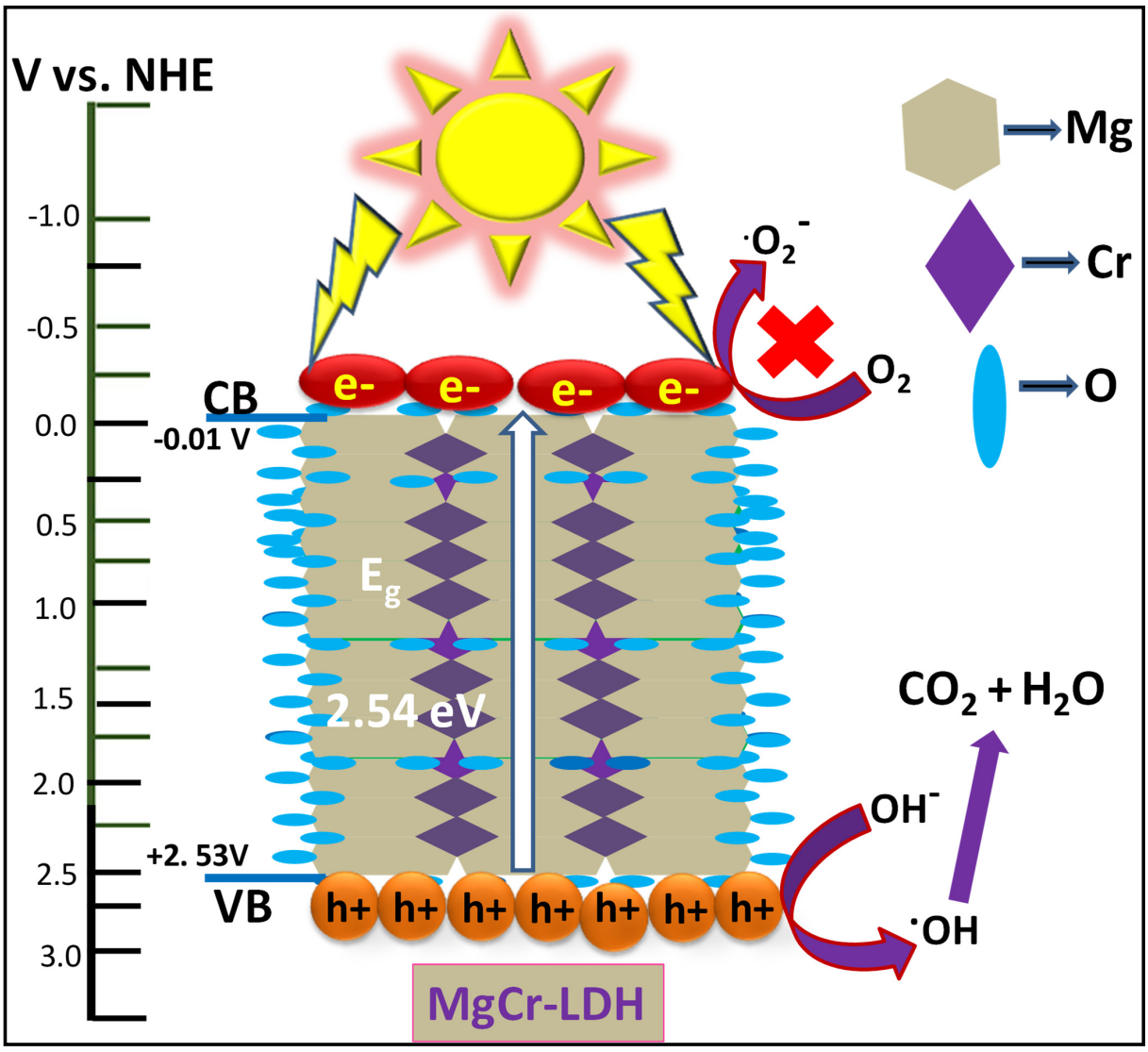

Figure 8. Plausible mechanism of charge separation by MgCr−LDH (3:1, 80 °C) for photocatalytic RhB degradation.

Based on the activities in scavengers test along with band edge position, the mechanism of charge separation in MgCr-LDH (3:1, 80 °C) for enhanced RhB degradation could be explained by following Equations (5)–(8):

$$MgCr + h\nu \rightarrow MgCr\ (h^+) + MgCr\ (e^-) \quad (5)$$

$$OH^- + MgCr\ (h^+)_{VB} \rightarrow \bullet OH \quad (6)$$

$$MgCr\ (h^+) + H_2O \rightarrow \bullet OH + H^+ \quad (7)$$

$$RhB + \bullet OH \rightarrow \text{several steps} \rightarrow \text{non-toxic products} \quad (8)$$

3. Experimental Section

3.1. Chemicals

$Mg(NO_3)_2{\cdot}6H_2O$ (98%, Sigma–Aldrich, India), and $Cr(NO_3)_3{\cdot}9H_2O$ (98%, Sigma–Aldrich), 23 vol% formamide (Sigma–Aldrich), anhydrous NaOH (98%, Sigma–Aldrich), were directly used for reaction. The mixed metal salt solutions were prepared by using deionized water.

3.2. Synthesis of Exfoliated MgCr-LDH NS by Formamide Method (2:1, 3:1, and 4:1)

Firstly, exfoliated MgCr-LDH gel was synthesized by co-precipitation method. In a distinct synthetic process, 20 mL of solution of mixed metal nitrate containing Mg $(NO_3)_2{\cdot}6H_2O$ (0.020 M) with Cr $(NO_3)_3{\cdot}9H_2O$ (0.010 M), Mg $(NO_3)_2{\cdot}6H_2O$ (0.030 M) with Cr $(NO_3)_3{\cdot}9H_2O$ (0.010 M), and Mg $(NO_3)_2{\cdot}6H_2O$ (0.040 M) with Cr $(NO_3)_3{\cdot}9H_2O$ (0.010 M) were drop-wise added to the specific quantity of 23 vol% formamide. The pH adjustment of the mixed metal solution was varied to pH 7 by slow addition of aqueous 1-M NaOH solution till the saturation of the precipitate of MgCr-LDH. The MgCr-LDH gel precipitate was again diffused in formamide solution and subsequently ultra-sonicated for 30 min. Afterwards, the MgCr-LDH (3:1) gel suspension was transferred into 100 mL Teflon lined autoclave reactor and treated at 70, 80, and 90 °C for 24 h. Then the product was centrifuged and washed 3–4 times with distilled H2O and vacuum dried at 40 °C. The coded name of the dried MgCr-LDHs samples at different atomic ratio are MgCr (2:1), MgCr (3:1), and MgCr (4:1), respectively. In addition, MgCr-LDH (2:1, 3:1, 4:1) without hydrothermal treatment was prepared for comparison.

3.3. Photocatalytic RhB Degradation Activity

(Conditions: exfoliated MgCr-LDH = 0.03 g, [RhB] = 20 ppm, exposer time = 120 min).

The photodegradation of RhB was executed in batch mode using a 20-ppm-concentrated RhB aqueous solution and 0.03 g of the catalyst. The suspension was uncovered to sunlight (~solar intensity = 0.80 kW/m^2) in closed Pyrex conical flasks with steady stirring during hot summer days. Prior to the solar experiments, dark reactions were carried out for comparison. The RhB degradation was analyzed by the spectrophotometric technique at 554 nm. After 2 h of solar irradiation, the conversion was reached up to 95.0%. Furthermore, the stability test of the catalyst for RhB degradation was repeated for three cycles. The stability test of the photocatalyst was executed in each run by simply washing with ethanol and deionized water followed by oven-drying at 80 °C for next use in second cycle.

3.4. Materials Characterization

Powder X-ray diffraction (PXRD) was performed by a Rigaku Miniflex powder diffraction meter, using Cu Kα source (λ = 1.54 Å, 30 kV, 50 mA). The bending and stretching modes of vibration of the materials were carried out by JASCO Fourier transform infrared (FTIR)-4600, using the KBr reference. The ultraviolet-visible diffuse reflectance spectra (UV−Vis DRS) were produced by a JASCO-V-750 UV−Vis spectrophotometer using $BaSO_4$ as a reference. Photoluminescence (PL) was analyzed using an FP-8300 JASCO spectrofluorometer. A high-resolution transmission electron microscopy (HR-TEM) and energy dispersive X-ray (EDX) study was carried by JEM-2100F at an accelerating voltage of 200 kV. The field emission scanning electron microscopy (FESEM) micrograph was acquired by a HITACHI 3400N microscope. The entire photoelectrochemical (PEC) measurements were carried out by potentiostat−galvanostat (IVIUM n STAT multi-channel electrochemical analyzer), with accessories of a 300 W Xenon lamp for visible light supply, a three-electrode system containing Pt, Ag/AgCl, and fluorine-doped tin oxide (FTO), as a counter, reference, and working electrode, respectively. The working electrode was made by an electrophoretic deposition process by our earlier reported method [15]. The electrolyte contained 0.1 M of Na_2SO_4 solution. The linear sweep voltammetry (LSV) study was completed by applied bias within −1.0 to +1.2 V at scanning rate of 5 mV s^{-1} in visible light exposure.

4. Conclusions

In summary, our thorough investigations on MgCr-(NO_3^-) LDH disclosed the exfoliation capability of MgCr-(NO_3^-) LDH in formamide into uni/multi-layer NS, which strongly depended on layer charge (Mg^{2+}/Cr^{3+} = 2:1, 3:1, and 4:1) and hydrothermal temperature (70, 80, and 90 °C). With an optimum metallic (Mg^{2+}/Cr^{3+}) ratio of 3:1, and hydrothermal treatment of 80 °C for 24 h, the exfoliated MgCr-(NO_3^-) LDH, displayed superior photocatalytic RhB degradation (95.0%) under solar light exposure for 2 h. This synthetic process is simple, cost-effective and thus potential strategy for the production of stable and exfoliated MgCr-LDH into uni/multi-layer NS. Finally, the morphology is a vital aspect in determining the nanosheet structure and by applying an optimized synthetic protocol; we tried to maintain house-of-nano-platelet morphology in MgCr-(NO_3^-) LDH (3:1, 80 °C) for light absorption, fast charge separation, and transfer for superior catalytic activities. Consequently, post-hydrothermal treatment might be suitable to augment productivity in exfoliation procedure. This work is an effectual approach to optimize novel catalytic system with high efficiency and stability, but initiate new ground for the vast application of MgCr-LDH in environmental remediation as well as energy production.

Author Contributions: S.N. and K.P. conceptualized and designed the experiments. S.N. synthesized the materials, executed the experiments, wrote, and edited the manuscript. All authors have read and agreed to the published version of the manuscript.

Funding: This research received no external funding.

Institutional Review Board Statement: Ethical review and approval were waived for this study.

Informed Consent Statement: Not applicable.

Data Availability Statement: Data sharing is not applicable to this article.

Acknowledgments: The authors gratefully acknowledge the support of the management of Siksha 'O' Anusandhan Deemed to be University to carry out this research work. The author S. Nayak is gratefully acknowledged to the CSIR-India for awarding CSIR-RA fellowship vide file no. 09/969 (0011)/2020 EMR-1 dated 13/10/2020.

Conflicts of Interest: The authors declare no conflict of interest.

References

1. Brisebois, P.P.; Siaj, M. Harvesting graphene oxide–years 1859 to 2019: A review of its structure, synthesis, properties and exfoliation. *J. Mater. Chem. C* **2020**, *8*, 1517–1547. [CrossRef]
2. Sultana, S.; Mansingh, S.; Parida, K.M. Facile synthesis of CeO_2 nanosheets decorated upon BiOI microplate: A surface oxygen vacancy promoted Z-scheme-based 2D-2D nanocomposite photocatalyst with enhanced photocatalytic activity. *J. Phys. Chem. C* **2018**, *122*, 808–819. [CrossRef]
3. Sakita, A.M.P.; Vallés, E.; Della Noce, R.; Benedetti, A.V. Novel NiFe/NiFe-LDH composites as competitive catalysts for clean energy purposes. *Appl. Surf. Sci.* **2018**, *447*, 107–116. [CrossRef]
4. Liang, D.; Yue, W.; Sun, G.; Zheng, D.; Ooi, K.; Yang, X. Direct synthesis of unilamellar MgAl-LDH nanosheets and stacking in aqueous solution. *Langmuir* **2015**, *31*, 12464–12471. [CrossRef]
5. Nayak, S.; Parida, K.M. Superactive NiFe-LDH/graphene nanocomposites as competent catalysts for water splitting reactions. *Inorg. Chem. Front.* **2020**, *7*, 3805–3836. [CrossRef]
6. Nayak, S.; Parida, K.M. Nanostructured CeO_2/MgAl-LDH composite for visible light induced water reduction reaction. *Int. J. Hydrog. Energy* **2016**, *41*, 21166–21180. [CrossRef]
7. Nayak, S.; Pradhan, A.C.; Parida, K.M. Topotactic transformation of solvated MgCr-LDH nanosheets to highly efficient porous MgO/$MgCr_2O_4$ nanocomposite for photocatalytic H2 evolution. *Inorg. Chem.* **2018**, *57*, 8646–8661. [CrossRef]
8. Nayak, S.; Parida, K. Comparison of NiFe-LDH based heterostructure material towards photocatalytic rhodamine B and phenol degradation with water splitting reactions. *Mater. Today Proc.* **2021**, *35*, 43–246. [CrossRef]
9. Nayak, S.; Parida, K. Recent progress in LDH@graphene and analogous heterostructure for highly active and stable photocatalytic and photoelectrochemical water splitting. *Chem. Asian J.* **2021**, *16*, 2211–2248. [CrossRef]
10. Sahoo, D.P.; Nayak, S.; Reddy, K.H.; Martha, S.; Parida, K. Fabrication of a $Co(OH)_2$/ZnCr LDH "p–n" heterojunction photocatalyst with enhanced separation of charge carriers for efficient visible-light-driven H_2 and O_2 evolution. *Inorg. Chem.* **2018**, *57*, 3840–3854. [CrossRef]

11. Nayak, S.; Mohapatra, L.; Parida, K. Visible light-driven novel g-C_3N_4/NiFe-LDH composite photocatalyst with enhanced photocatalytic activity towards water oxidation and reduction reaction. *J. Mater. Chem. A* **2015**, *3*, 18622–18635. [CrossRef]
12. Nayak, S.; Parida, K.M. Dynamics of charge-transfer behavior in a plasmon-induced quasi-type-II p–n/n–n dual heterojunction in Ag@ Ag_3PO_4/g-C_3N_4/NiFe LDH nanocomposites for photocatalytic Cr(VI) reduction and phenol oxidation. *ACS Omega* **2018**, *3*, 7324–7343. [CrossRef] [PubMed]
13. Nayak, S.; Parida, K.M. Deciphering Z-scheme charge transfer dynamics in heterostructure NiFe-LDH/N-rGO/g-C_3N_4 nanocomposite for photocatalytic pollutant removal and water splitting reactions. *Sci. Rep.* **2019**, *9*, 2458–2481. [CrossRef]
14. Biswal, L.; Nayak, S.; Parida, K. Recent progress on strategies for the preparation of 2D/2D MXene/g-C_3N_4 nanocomposites for photocatalytic energy and environmental applications. *Catal. Sci. Technol.* **2021**, *11*, 1222–1248. [CrossRef]
15. Nayak, S.; Swain, G.; Parida, K. Enhanced photocatalytic activities of RhB degradation and H2 evolution from in situ formation of the electrostatic heterostructure MoS_2/NiFe LDH nanocomposite through the Z-scheme mechanism via p–n heterojunctions. *ACS Appl. Mater. Interfaces* **2019**, *11*, 20923–20942. [CrossRef]
16. Gholami, P.; Khataee, A.; Soltani, R.D.C.; Dinpazhoh, L.; Bhatnagar, A. Photocatalytic degradation of gemifloxacin antibiotic using Zn-Co-LDH@ biochar nanocomposite. *J. Hazard. Mater.* **2020**, *382*, 121070–121081. [CrossRef] [PubMed]
17. Wang, Q.; O'Hare, D. Recent advances in the synthesis and application of layered double hydroxide (LDH) nanosheets. *Chem. Rev.* **2012**, *112*, 4124–4155. [CrossRef]
18. Ma, R.; Liu, Z.; Li, L.; Iyi, N.; Sasaki, T. Exfoliating layered double hydroxides in formamide: A method to obtain positively charged nanosheets. *J. Mater. Chem. A* **2006**, *16*, 3809–3813. [CrossRef]
19. Hibino, T.; Jones, W. New approach to the delamination of layered double hydroxides. *J. Mater. Chem. A* **2001**, *11*, 1321–1323. [CrossRef]
20. Karthikeyan, J.; Fjellvåg, H.; Knudsen, K.; Vistad, Ø.B.; Sjåstad, A.O. Quantification and key factors in delamination of $(Mg_{1-y}Ni_y)_{1-x}Al_x(OH)_2(NO_3)_x \cdot mH_2O$. *Appl. Clay Sci.* **2016**, *124–125*, 102–110. [CrossRef]
21. Li, L.; Ma, R.; Ebina, Y.; Iyi, N.; Sasaki, T. Positively charged nanosheets derived via total delamination of layered double hydroxides. *Chem. Mater.* **2005**, *17*, 4386–4391. [CrossRef]
22. Wu, Q.; Olafsen, A.; Vistad, Ø.B.; Roots, J.; Norby, P. Delamination and restacking of a layered double hydroxide with nitrate as counter anion. *J. Mater. Chem. A* **2005**, *15*, 4695–4700. [CrossRef]
23. Adachi-Pagano, M.; Forano, C.; Besse, J.-P. Delamination of layered double hydroxides by use of surfactants. *Chem. Commun.* **2000**, *1*, 91–92. [CrossRef]
24. Hibino, T. Delamination of layered double hydroxides containing amino acids. *Chem. Mater.* **2004**, *16*, 5482–5488. [CrossRef]
25. Liang, H.; Meng, F.; Cabán-Acevedo, M.; Li, L.; Forticaux, A.; Xiu, L.; Wang, Z.; Jin, S. Hydrothermal continuous flow synthesis and exfoliation of NiCo layered double hydroxide nanosheets for enhanced oxygen evolution catalysis. *Nano Lett.* **2015**, *15*, 1421–1427. [CrossRef] [PubMed]
26. Acharya, L.; Nayak, S.; Pattnaik, S.P.; Acharya, R.; Parida, K. Resurrection of boron nitride in pn type-II boron nitride/B-doped-g-C_3N_4 nanocomposite during solid-state Z-scheme charge transfer path for the degradation of tetracycline hydrochloride. *J. Colloid Interface Sci.* **2020**, *566*, 211–223. [CrossRef]
27. Yu, J.; Liu, J.; Clearfield, A.; Sims, J.E.; Speiegle, M.T.; Suib, S.L.; Sun, L. Synthesis of layered double hydroxide single-layer nanosheets in formamide. *Inorg. Chem.* **2016**, *55*, 12036–12041. [CrossRef]
28. Yu, J.; Martin, B.R.; Clearfield, A.; Luo, Z.; Sun, L. One-step direct synthesis of layered double hydroxide single-layer nanosheets. *Nanoscale* **2015**, *7*, 9448–9451. [CrossRef]
29. Sharma, S.K.; Kushwaha, P.K.; Srivastava, V.K.; Bhatt, S.D.; Jasra, R.V. Effect of hydrothermal conditions on structural and textural properties of synthetic hydrotalcites of varying Mg/Al ratio. *Ind. Eng. Chem. Res.* **2007**, *46*, 4856–4865. [CrossRef]
30. Yang, X.; Makita, Y.; Liu, Z.-h.; Sakane, K.; Ooi, K. Structural characterization of self-assembled MnO_2 nanosheets from birnessite manganese oxide single crystals. *Chem. Mater.* **2004**, *16*, 5581–5588. [CrossRef]
31. Cavani, F.; Trifiro, F.; Vaccari, A. Hydrotalcite-type anionic clays: Preparation, properties and applications. *Catal. Today* **1991**, *11*, 173–301. [CrossRef]
32. Kustrowski, P.; Sulkowska, D.; Chmielarz, L.; Rafalska-Lasocha, A.; Dudek, B.; Dziembaj, R. Influence of thermal treatment conditions on the activity of hydrotalcite-derived Mg-Al oxides in the aldol condensation of acetone. *Microporous Mesoporous Mater.* **2005**, *78*, 1–22. [CrossRef]
33. Abello, S.; Medina, F.; Tichit, D.; Ramirez, J.P.; Groen, J.C.; Sueiras, J.E.; Salagre, P.; Cesteros, Y. Aldol condensations over reconstructed Mg-Al hydrotalcites: Structure-activity relationships related to the rehydration method. *Chem. A Eur. J.* **2005**, *11*, 728–739. [CrossRef] [PubMed]
34. Yin, W.; Bai, L.; Zhu, Y.; Zhong, S.; Zhao, L.; Li, Z.; Bai, S. Embedding metal in the interface of a p-n heterojunction with a stack design for superior Z-scheme photocatalytic hydrogen evolution. *ACS Appl. Mater. Interfaces* **2016**, *8*, 23133–23142. [CrossRef] [PubMed]
35. Ye, L.; Deng, K.; Xu, F.; Tian, L.; Peng, T.; Zan, L. Increasing visible-light absorption for photocatalysis with black BiOCl. *Phys. Chem. Chem. Phys.* **2012**, *14*, 82–85. [CrossRef] [PubMed]
36. Aguirre, M.E.; Zhou, R.; Eugene, A.J.; Guzman, M.I.; Grel, M.A. Cu_2O/TiO_2 heterostructures for CO_2 reduction through a direct Z-scheme: Protecting Cu_2O from photocorrosion. *Appl. Catal. B* **2017**, *217*, 485–493. [CrossRef]

37. Zeng, H.; Zhang, W.; Deng, L.; Luo, J.; Zhou, S.; Liu, X.; Pei, Y.; Shi, Z.; Crittenden, J. Degradation of dyes by peroxymonosulfate activated by ternary CoFeNi-layered double hydroxide: Catalytic performance, mechanism and kinetic modeling. *J. Colloid Interface Sci.* **2018**, *515*, 92–100. [CrossRef]
38. Zhao, X.; Niu, C.; Zhang, L.; Guo, H.; Wen, X.; Liang, C.; Zeng, G. Co-Mn layered double hydroxide as an effective heterogeneous catalyst for degradation of organic dyes by activation of peroxymonosulfate. *Chemosphere* **2018**, *204*, 11–21. [CrossRef] [PubMed]